

**REPORT DOCUMENTATION PAGE**Form Approved  
OMB No. 0704-0188

Public reporting burden for this collection of information is estimated to average 1 hour per response, including the time for reviewing instructions, searching data sources, gathering and maintaining the data needed, and completing and reviewing the collection of information. Send comments regarding this burden estimate or any other aspect of this collection of information, including suggestions for reducing this burden to Washington Headquarters Service, Directorate for Information Operations and Reports, 1215 Jefferson Davis Highway, Suite 1204, Arlington, VA 22202-4302, and to the Office of Management and Budget, Paperwork Reduction Project (0704-0188) Washington, DC 20503.

**PLEASE DO NOT RETURN YOUR FORM TO THE ABOVE ADDRESS.**

<b>1. REPORT DATE (DD-MM-YYYY)</b> 06-10-2003		<b>2. REPORT DATE Type</b> FINAL		<b>3. DATES COVERED (From - To)</b> 07-Jan-99 to 06-Jun-02	
<b>4. TITLE AND SUBTITLE</b> A Doppler Sensor Array for High-Resolution Measurements of the Wavenumber-Frequency Spectrum of the Turbulent Wall Pressure at High Reynolds Numbers				<b>5a. CONTRACT NUMBER</b> NA	
				<b>5b. GRANT NUMBER</b> N00014-99-10858	
				<b>5c. PROGRAM ELEMENT NUMBER</b> NA	
				<b>5d. PROJECT NUMBER</b> NA	
<b>6. AUTHOR(S)</b>  Ahmed M. Naguib				<b>5e. TASK NUMBER</b> NA	
				<b>5f. WORK UNIT NUMBER</b> NA	
<b>7. PERFORMING ORGANIZATION NAME(S) AND ADDRESS(ES)</b> Michigan State University Mechanical Engineering Department C128 Research Complex East Lansing, MI 48824				<b>8. PERFORMING ORGANIZATION REPORT NUMBER</b>  NA	
<b>9. SPONSORING/MONITORING AGENCY NAME(S) AND ADDRESS(ES)</b> Office of Naval Research Ballston Centre Tower One 800 N. Quincy St. Arlington, VA 22217-5660				<b>10. SPONSOR/MONITOR'S ACRONYM(S)</b> ONR	
				<b>11. SPONSORING/MONITORING AGENCY REPORT NUMBER</b>	
<b>12. DISTRIBUTION AVAILABILITY STATEMENT</b>  Approved for Public Release; Distribution is Unlimited					
<b>13. SUPPLEMENTARY NOTES</b>  None					
<b>14. ABSTRACT</b> The Doppler frequency shift is utilized as the basic sensing mechanism for a new unsteady-surface pressure measurement technique. The frequency shift is experienced by a focused laser beam reflected off the aluminized top of a flexible polymer diaphragm subjected to the unsteady pressure. Prototypical sensors based on this concept, with different sizes and diaphragm material and thickness are constructed as well as evaluated. The results provide understanding of the limits of the sensor's sensitivity, bandwidth, resolution and noise-level. Moreover, analysis of typical wall-pressure spectra beneath high- and low-Reynolds-number boundary layers in light of these limits underlines the potential advantage of the new sensor in resolving the signature of small-scale turbulent structures at high Reynolds numbers.					
<b>15. SUBJECT TERMS</b>  Wall Pressure; Hydrophones; Doppler; Sensor Array					
<b>16. SECURITY CLASSIFICATION OF:</b>			<b>17. LIMITATION OF ABSTRACT</b>  SAR	<b>18. NUMBER OF PAGES</b>  45	<b>19a. NAME OF RESPONSIBLE PERSON</b> Ahmed M. Naguib
<b>a. REPORT</b>	<b>b. ABSTRACT</b>	<b>c. THIS PAGE</b>			<b>19b. TELEPHONE NUMBER (Include area code)</b> (517) 432-1616

## TABLE OF CONTENTS

<b>I. INTRODUCTION</b>	<b>2</b>
<b>II. OBJECTIVES</b>	<b>4</b>
<b>III. DETAILS OF SENSOR SYSTEM</b>	<b>5</b>
<b>IV. SENSOR CALIBRATION</b>	<b>9</b>
<b>V. OPERATING CONSIDERATIONS</b>	<b>11</b>
<b>VI. SENSOR CHARACTERISTICS</b>	<b>15</b>
<b>VII. CONCLUSIONS</b>	<b>24</b>
<b>VIII. ACKNOWLEDGEMENT</b>	<b>25</b>
<b>IX. FIGURES</b>	<b>26</b>
<b>X. REFERENCES</b>	<b>44</b>

20031010 090

## I. INTRODUCTION

This document is submitted as a final report on the development and testing of a new unsteady-surface-pressure Doppler sensor (hereafter referred to as LDH/LDM, or Laser Doppler Hydrophone/Microphone) for high-resolution measurements at high Reynolds number in water/air flows. Most of this document has also appeared in a recent journal publication by Daoud and Naguib (2003). Additionally, a comprehensive two-year report was submitted at the end of the first two years to the program manager, Dr. Patrick Purtell, for evaluation and decision on optional third-year funds to use an array of LDH sensors for high-Reynolds-number measurements in the Navy's Large Cavitation Channel (LCC). Third-year funding was not provided, and therefore no measurements were conducted in the LCC. However, the outcome of the detailed analysis over the first two years is used to project the suitability of the new sensing method for measurements at high Reynolds number in general, and in the LCC in particular, in section *VI.F* of this document.

Measurement of the unsteady surface pressure signature produced by a wide range of turbulent flows is significant for a number of reasons. For example, understanding and predicting flow and structure behavior in applications involving flow/structure interaction in general, and flow-induced vibrations in particular, depend on knowledge of the normal flow stresses acting on the surface. Another example pertain to the use of array measurements of the surface pressure to obtain the wall vorticity flux: a quantity that is important not only for interpretation of flow physics but also for flow computation using vortex methods.

When it comes to sensing the surface pressure at high Reynolds numbers, current techniques are generally limited by their spatial resolution. In particular, at Reynolds numbers comparable to those encountered over a ship, submarine, or airplane, the turbulent boundary

layer viscous length scale ( $\nu/u_\tau$ ;  $\nu$  being the kinematic viscosity and  $u_\tau$  is the friction velocity) is typically as small as a few to tens of microns. Gravante *et al.* (1998) showed that a non-dimensional sensor diameter ( $d^+ = du_\tau/\nu$ ) of 18 or smaller is sufficient to resolve the influences of the wall-pressure-producing eddies. Thus, sensors with diameters of 0.5mm or less are generally required to fully resolve the wall-pressure signature in typical high-Reynolds-number test facilities. Additionally, if it is desired to measure maps of the wall-vorticity flux, a sensor array with small inter-sensor spacing is required in order to accurately estimate the spatial gradients of the surface pressure. The cost and implementation complexity of such an array should also be kept to a minimum if the measurement technique is to be viable and of practical use.

The work presented here is aimed at assessment of a laser Doppler microphone (LDH) concept. Because a laser beam can be focused to a spot size of a few to tens of microns, very high spatial resolution can be potentially obtained with the new sensor. Other attractive features of the LDH include:

- Usability in applications requiring in-line sensor arrays with small inter-sensor spacing.
- Ability to extract the sensor output without physical contact with the test model. This feature is particularly useful for array applications, where one would otherwise need to provide provisions for passage of myriad of wires through the test model. The same feature also renders the LDH usable for pressure measurements on moving surfaces.
- Feasibility to implement the technique using fiber optics, which enables electromagnetic-interference-free data transmission over long distances.

Existing optical-based acoustic sensors are primarily of the fiber-optic type. Those may be classified into intrinsic and extrinsic (Hixson and Bush-Vishniac, 1998). In the former, light

never leaves the fiber and the sensing principle is typically based on Mach-Zender interferometry (see Bucaro *et al.* (1982) for details). On the other hand, in extrinsic fiber-optic sensors, light leaves the fiber and reflects off a target that is moving under the action of the sound pressure. In most instances, the intensity of the reflected light is modulated by, and hence is proportional to, the acoustic pressure. This is known as the lever-type microphone (He and Cuomo, 1991). In contrast to the intrinsic microphones, the lever-type sensors can be made with a fairly small sensing diameter. A good example may be found in the work of Zuckerwar *et al.* (1995), who developed and tested a 1.8mm-diameter fiber-optic lever microphone for use in harsh high-temperature environments.

Unlike both the Mach-Zender and lever sensors, the LDH does not require optical fibers for its operation and hence it can be used for non-contact, 'point-and-shoot' measurements. Also, since the measured pressure is proportional to the output signal frequency, rather than magnitude, the sensor is generally less prone to noise at low-pressure levels. Finally, the LDH is believed to possess the potential for achieving significantly higher spatial resolution than the lever-type microphone because of the limitation imposed by the minimum fiber-optic size on the latter (see Zukerwar *et al.*, 1995).

## II. OBJECTIVES

In this paper, the use of the Doppler frequency shift as a basis for measurement of the unsteady surface pressure is proposed. Several prototype sensors are constructed and the technique is evaluated in terms of its realizability, sensitivity, resolution, bandwidth, accuracy and background noise. Furthermore, results of the evaluation tests are used to assess the utility of the LDH to measure wall-pressure fluctuations beneath high-Reynolds-number turbulent boundary layers. It should be noted here that although not investigated in this study, a complete

characterization of the sensor response should include examination of the effect of temperature on sensor response. This is left to a future study.

### III. DETAILS OF SENSOR SYSTEM

*III.A. Concept and Construction.* The primary sensing element of the LDH consists of a thin polymer diaphragm with a reflective upper surface attached to a plug substrate on top of a hole, as seen in Figure 1. Under the action of the unsteady flow pressure, the diaphragm experiences time-dependent deflection on top of the hole (note that the spatial resolution of the sensor is thus determined by the hole diameter,  $d$ ). The instantaneous wall-normal velocity ( $v(t)$ ) of the diaphragm is measured using the Doppler frequency shift of a laser beam incident on the reflective side of the pressure-sensing foil. The corresponding deflection ( $x(t)$ ) is obtained from integration of  $v(t)$ . Since the wall pressure ( $p(t)$ ) acting on the diaphragm is directly proportional to  $x$ , within the elastic limit of the diaphragm and its bandwidth, one may obtain  $p$  from:

$$p(t) = \frac{1}{K_x} \int v(t) dt + p_o \quad [1]$$

where  $K_x$  is the deflection static sensitivity of the diaphragm (typically in units of  $\mu\text{m}/\text{Pa}$ ) and  $p_o$  is an integration constant equal to the local mean surface pressure.

It should be mentioned here that Emmerling (1973) constructed a 2.5mm-diameter sensor array with 3mm inter-sensor spacing using 30 $\mu\text{m}$  polymer diaphragm on top of a hole array. Unlike the current study, however, Emmerling used spatial interferometry to measure the foil deflection directly. This method of detecting foil deflection requires foil surface that is flat within a fraction of a wavelength and fairly large foil deflections. Moreover, spatial interferometry is not suitable for measurement over the minute area of sub-mm sensors.

Figure 2 shows a schematic of the sensor faceplate design and how it is installed inside the calibration setup (explained later in section IV). A piece of foil is attached to the top of the

faceplate using the adhesion force of water. The basic idea here is to moisten the top of the faceplate with water and place the piece of foil gently on top of the water. The water then spreads between the foil and faceplate, stretching the foil to form a flat sensing surface. The resulting stretching force is minimal because it results from water adhesion effects only.

The faceplate is made out of Plexiglass since it produces both a nice flat foil surface and firm adhesion force with water to hold the foil in place. Both foil sensitivity and its surface quality stay stable over a period of few hours. Over a longer 48-hour period, a change within 10% in sensor sensitivity is typically observed. The use of water as a 'bonding' material, rather than epoxy or glue, enabled the attainment of low diaphragm stretching forces and construction of sensors with various diameters, materials, thickness, etc, easily, which suited the purposes of the current parametric investigation. In practice, however, more robust methods, including microfabrication techniques, could be developed for appropriate construction of single or multi-sensor units for use outside the laboratory. Those methods are not part of the current study, which is primarily concerned with the evaluation of the LDH concept.

In this paper, four different faceplates with sensor hole diameters of  $d = 6.35, 3.175, 1.5875,$  and  $0.794\text{mm}$  (corresponding to  $d = 1/4, 1/8, 1/16,$  and  $1/32''$ ) are used. Moreover, two different foil materials and three thicknesses are utilized. One of the materials is PolyEthylene Terephthalate (PET) film, which has a tensile modulus in the range  $2 - 4\text{GPa}$ . The other material is Polypropylene (PP), the tensile modulus of which is in the range  $0.9-1.5\text{GPa}$ , and therefore is more flexible than PET by a factor of  $1.3 - 4$ . Both materials are available commercially from Goodfellow in various thicknesses with an aluminum layer of approximately  $10\text{nm}$  deposited on one side of the foil. The corresponding foil thicknesses used here are  $5$  and  $12\mu\text{m}$  for PET and

8 $\mu$ m for PP. The aluminum side of the foil, which has a mirror-like finish, is used to reflect the laser beam for the Doppler measurements.

*III.B. Optical System.* A picture of the optical system used to generate the Doppler signal and a corresponding ray-trace schematic are provided in Figure 3. The light source for the Doppler system is a uniphase 20mW polarized He-Ne laser with a wavelength ( $\lambda$ ) of 633nm. The laser beam passes through a  $\frac{1}{4}\lambda$  plate (QP), which in combination with the laser head polarizer stops any reflected laser light from entering the laser tube. After the  $\frac{1}{4}\lambda$  plate, the laser beam is split into 'measurement' and 'reference' beams (sketched using solid and broken lines, respectively, in Figure 3) using 50/50 cube beam splitter (BS1). Each of these two beams is passed through an International Corp. acousto-optic modulator, model AOM-40, for independent frequency biasing to eliminate the sign ambiguity of the Doppler frequency shift. The acousto-optic modulators are driven using an Interaction Corp. dual-channel frequency synthesizer, model DFE. The use of two independent AOM units enables the attainment of a frequency bias between the measurement and the reference beams in steps of  $\pm 10$ kHz. Furthermore, the single-crystal driver of both units ensures temperature-independent frequency shift. The frequency-shifted measurement beam is directed towards the LDH diaphragm through a second beam splitter (BS2), off mirrors M1, M2 and M3, and through a 250mm focal length achromatic lens (AL), which is used to decrease the spot size of the beam to approximately 0.4mm.

On the other hand, the reference beam is reflected off a number of mirrors (M4 through M8) to redirect it towards BS2 (see Figure 3), where it recombines with the measurement beam *after* reflection from the pressure sensor foil. The use of multiple mirrors to redirect the reference beam enables adjustment of the optical path length of the beam to ensure that the mismatch in path length of both beams is within the coherence length of the laser. Finally, both



beams are mixed ('heterodyned') on the surface of a low-noise Photodetector (PD), after passing through a pinhole (PH) for minimizing extraneous light effect.

It is interesting to note here that the frequency shift for the same membrane velocity could be doubled by using a variation of the system described above. More specifically, by directing the beam at an angle of, say,  $90^\circ - \alpha$ , it would reflect off the membrane at  $90^\circ + \alpha$ . A mirror placed in the path of the reflected beam, would send the beam back towards the membrane causing a 'double reflection' before mixing with the reference beam on the photo detector surface.

*III.C. Doppler-Frequency Detection.* To measure the frequency of the photodetector signal, an FFT-based approach is used. The signal is acquired using a 12-bit, 50 Mega samples/s, two-channel, one-Mega-sample-data-memory, Gagescope CS1250 data acquisition card from Gage. In the traditional FFT approach, the power spectrum of each data record of the photodetector signal is computed using the FFT. Subsequently, the Doppler frequency is determined to be that corresponding to the maximum spectrum magnitude. The resolution by which the Doppler frequency ( $f_D$ ) is determined using the spectrum peak technique is given by  $\Delta f_D = 1/T_{\text{rec}}$ , where  $T_{\text{rec}}$  is the duration of the acquired photodetector signal. Typically 512-point data records were acquired at 5 MHz, resulting in  $T_{\text{rec}}$  of 102.4  $\mu\text{s}$ , or  $\Delta f_D = 9766$  Hz. The corresponding velocity resolution ( $\Delta v = \lambda \Delta f_D / 2$ ) is approximately 3 mm/s. Note that since every data record yields one Doppler frequency, and hence a single velocity data point, the sampling of velocity information can't be achieved at a rate larger than  $1/T_{\text{rec}} = 9.766$  kHz. Hence, if it is desired to enhance the measurement resolution by increasing  $T_{\text{rec}}$ , one must sacrifice the data bandwidth. Resolution issues are discussed in further detail in section V.A.

#### IV. SENSOR CALIBRATION

A Plane Wave Tube (PWT) is used to obtain the frequency response of the LDM. Basically, a PWT produces plane sound waves that travel parallel to the axis of a tube or a duct. This one-dimensional planar wave propagation is realized if the width of the duct is small in comparison to the acoustic wavelength ( $\lambda_a$ ). In particular, for a square duct with rigid walls and side length of  $2a$ , planar wave propagation is accomplished when  $\lambda_a > 4a$ , or  $f < c/4a$  (where  $f$  is the sound frequency and  $c$  is the speed of sound); e.g., Kinsler *et al.* (1982). Thus,  $f = c/4a$  establishes the upper limit, or cut-off, frequency of the PWT. In the current investigation, the PWT width selected is 31.75mm, which gives an upper frequency limit of approximately 5500Hz for a speed of sound of 350m/s.

A picture of the acoustic-wave-guide setup may be seen in the picture in Figure 3. A corresponding schematic diagram is provided in Figure 2. The tube is made of 1.5m long aluminum square duct with a cross-section of  $31.75 \times 31.75\text{mm}^2$  and a wall thickness of 3.175mm. The center of the sensor plug is located at a distance of 750mm from each of the PWT ends. At the same cross section, a hole for mounting a reference Panasonic WM-61A microphone (with known response) is made in the lower wall of the PWT (see Figure 2 and inset in Figure 3). A length of 50.8mm of the PWT wall opposite to the sensor plug was removed and replaced with a plexiglass window of the same thickness as the PWT wall. This window, which was flush with the inside wall of the PWT, enabled optical access for conducting the Doppler measurements.

Before using the PWT for calibration purposes, it is necessary to check the accuracy of the calibration procedure. The test is conducted using two Panasonic microphones with known response. The first microphone is positioned in the PWT floor inside the reference microphone

hole, while the second one is mounted in the sensor plug in place of the LDM using a special adapter ring. In this fashion, it is possible to conduct measurements at the LDM and reference microphone locations to verify that the sound pressure level and phase at the test frequencies are the same at both locations.

It should be noted that the Panasonic microphones have a manufacturer specified frequency response that is flat between 20Hz and 20kHz. Frequency calibration of tens of these microphones (Hudy, 2001) has verified the flatness of the response of these microphones up to 5000Hz, and the linearity of their phase characteristics with a corresponding time delay of less than 20 $\mu$ s. Furthermore, the specific sensitivity value of the individual microphones used here was determined using Larson & Davis Precision Acoustic Calibrator (CAL200). For this purpose, a custom adaptor was made to ensure that the internal cavity volume of the calibrator was unchanged when mounting the Panasonic microphones.

Figure 4 shows the test results for frequency values of 60 to 9500Hz and 110dB sound pressure level (re 20 $\mu$ Pa). The figure represents the ratio of the *rms* pressure ( $R_p$ ) of the measured signals from the two microphones, and the corresponding phase difference ( $\phi$ ). The results show that  $R_p$  is approximately equal to one up to 5000Hz, Figure 4 (top). On the other hand, by inspecting the phase shift between the two microphones, which is plotted in degrees in Figure 4 (bottom), it is evident that the value of  $\phi$  is maintained within a few degrees up to a frequency of 5000Hz. Above this frequency, significant scatter starts to appear. Both the  $R_p$  and  $\phi$  results are consistent with the propagation of one-dimensional, planar sound waves in the PWT up to the predetermined design frequency ( $f \approx 5000$ Hz).

Because the foil deflection is highest at the center of the sensor hole, alignment of the measuring beam with this center yields the highest sensitivity. To accomplish the alignment, a

CCD camera coupled to a frame grabber is used to capture a magnified image of the sensor hole and beam spot on the foil from the backside. This image is used to locate the pixel coordinates corresponding to the center of the hole. The appropriate mirrors in the optical system are then manipulated to align the laser beam spot with this center within approximately  $\pm 5$  pixels. For the worst-case scenario ( $d = 0.794\text{mm}$ ), this error is estimated to be  $\pm 40\mu\text{m}$ , which corresponds to a percentage error of  $\pm 5\%$ . Figure 5 shows a sample image of an aligned beam spot.

## V. OPERATING CONSIDERATIONS

*V.A. Doppler Frequency Resolution.* The LDM's Doppler-frequency-resolution requirement is significantly more stringent than that available from off-the-shelf FFT-based Doppler systems for measurement of mechanical vibrations or flow velocity. Typically, current FFT-based systems are commonly used to measure low-speed, narrow-bandwidth velocities (e.g., water flows), or high-speed, wide-bandwidth ones (e.g., air flows). In the LDM case, the foil velocity is very low (fraction of a mm/s) and the desired bandwidth is wide (a few kHz). This requires high Doppler frequency resolution, or long data record time ( $T_{\text{rec}}$ ), which can't be reconciled with the desired wide bandwidth using existing FFT methods of Doppler frequency measurements. Appropriate modifications are needed for successful operation of the LDM.

Using computer generated signals, Naguib (2002) demonstrated that the resolution of locating the spectrum peak corresponding to the Doppler frequency in FFT-based methods can be enhanced significantly by using a centroid technique. In particular, he showed that by windowing sinusoidal data records using a Hanning function and employing a centroid method to locate the corresponding spectrum peak, the Doppler frequency can be determined with a resolution that is 10-50 times better than the traditional way, at signal-to-noise ratios of 10 – 20dB. For larger signal-to-noise ratios, even larger improvements are possible. Sample

measurements of the foil deflection ( $x$ ) conducted using the traditional (referred to as 'peak') and centroid FFT-based methods may be seen in Figure 6. The data in the figure were obtained by subjecting a 3.175mm LDM to 200Hz sound field in the PWT. Simultaneous measurements from the Panasonic reference microphone were utilized to estimate the actual foil deflection by dividing the microphone's pressure time-series by the foil's mechanical sensitivity ( $K_x$ ). Also note that the results in Figure 6 include data from the centroid analysis with and without the use of a Hanning window.

Figure 6 clearly shows that the existing FFT-based approach fails to accurately capture the foil deflection. Significant improvement is attained when using the centroid technique without windowing (i.e., with boxcar window). However, noticeable amplitude attenuation and harmonic distortion are still apparent. Only when the Hanning-window and centroid combination is used do the measured and actual deflection agree well.

Quantitative examination of the measurement error for the results in Figure 6 shows that when using the Hanning/centroid combination the error is less than 15% of the signal amplitude. This translates to a velocity error of approximately 40  $\mu\text{m/s}$ . When compared to the velocity resolution of 3 mm/s obtained from the traditional FFT (see section *III.C*), this error indicates a resolution enhancement by a factor of 75. All results reported in this paper are processed using the Hanning/centroid combination. Six FFT bins are employed in the centroid method, which include the bin corresponding to the maximum spectrum value and the two-higher- and three-lower-frequency bins.

*V.B. Method of Integration.* Because the foil deflection is determined from numerical integration of the velocity time series, the accuracy of the integration process depends on the time step size. Therefore, there was a concern that a substantial error might occur as the

velocity-signal frequency approaches the Nyquist frequency ( $f_N$ ), where the step size approaches half the signal period. To remedy this problem, a frequency-domain integration method was adopted. More specifically, it is well known that the frequency characteristics of an ideal integrator is given by:

$$\frac{X(\omega)}{V(\omega)} = \frac{1}{j\omega} = \frac{e^{-j\frac{\pi}{2}}}{\omega} \quad [2]$$

where,  $X$  and  $V$  are the Fourier transforms of the deflection and velocity, respectively,  $j = \sqrt{-1}$ , and  $\omega = 2\pi f$ . Thus, one may calculate the deflection from the velocity via a frequency-domain filtering approach. First, the velocity signal is fast Fourier transformed. The magnitude of the transformed values is then reduced by  $\omega$ , the phase angle is delayed by  $\pi/2$  and the result is inverse-transformed back to the time domain to yield the displacement time series.

One drawback of frequency-domain filtering is contamination of the displacement time series at both ends due to circular convolution effects. This contamination, however, is limited to a few points, and the problem may be easily remedied by acquiring longer time series and discarding the bad data points at the beginning and end.

*V.C. Noise Analysis.* Figure 7 displays foil velocity spectra (solid line) recorded when a 6.35mm (top plot) and 1.587mm (bottom plot) LDM Sensors were subjected to 100Hz sound wave in the plane wave tube. Also included in the figure are noise velocity spectra (broken line), which were obtained from the same sensors when the sound source was turned off. Examination of these noise spectra reveals that they are primarily composed of multiple narrow harmonic peaks and white noise. Additionally, a broad peak dominates the spectrum of the 6.35mm sensor for  $f > 1000\text{Hz}$ . This peak corresponds to the resonant frequency of this sensor (see Figure 13). On the other hand, the narrow harmonic peaks could be linked to environmental (as deduced

from concurrent measurements by the reference Panasonic microphone) and electronic noise (harmonics of 60 Hz). Since both of these noise sources do not pertain directly to the LDM (e.g., the latter type of noise could be minimized using battery operated electronics), it is apparent that the LDM's inherent velocity-noise spectrum is essentially flat, of the white-noise type (away from the sensor's resonant frequency). Moreover, the magnitude of this spectrum seems to decrease with decreasing sensor size. For example, for the 6.35mm sensor, this magnitude is approximately  $4\mu\text{m}^2/\text{s}^2$  ( $0.43\mu\text{m/s}/\sqrt{\text{Hz}}$ ), whereas for the 1.587mm sensor, the noise spectrum magnitude is  $0.1\mu\text{m}^2/\text{s}^2$  ( $0.01\mu\text{m/s}/\sqrt{\text{Hz}}$ ).

If the magnitude of the velocity noise spectrum is  $C_n^2$  then the displacement noise spectrum is given by  $C_n^2/(2\pi f)^2$ . This may be recast in terms of a noise equivalent pressure (NEP) spectrum as follows:

$$\text{NEP} = \left[ \frac{C_n}{2\pi K_x} \right]^2 \frac{1}{f^2} = \frac{P_n}{f^2} \quad [3]$$

where  $P_n$  is a constant for a particular sensor. Equation [3] clearly shows that the lower the frequency the larger the noise level. This is a result of the integration operation, which amplifies noise at lower frequencies (opposite to differentiation, which increases noise at higher frequencies).

Since  $C_n$  was found to be a function of  $K_x$ ,  $P_n$  in equation [3] should also be a function of the sensor's sensitivity. By estimating  $C_n$  from the noise spectra of the 1.587, 3.175 and 6.35mm sensors and knowing the corresponding  $K_x$  values from sensor calibration, it was possible to calculate  $P_n$  for the different sensor sizes. A plot of this quantity versus the sensor sensitivity is provided in Figure 8 on a log-log scale. The dependence of  $P_n$  on  $K_x$  appears to be reasonably

represented using a power law fit, which is used to obtain the following empirical formula for NEP:

$$\text{NEP} = \frac{0.05}{K_x^{0.94}} \frac{1}{f^2} \quad [4]$$

## VI. SENSOR CHARACTERISTICS

*VI.A. Sensitivity and Sensor-Size Effect.* To obtain the sensitivity of sensors of different diameters, the frequency of sound in the PWT was maintained at 200Hz while varying the *rms* sound pressure ( $p_{rms}$ ) over the range of approximately 1 – 10Pa. The resulting foil *rms* deflection was measured and plotted against  $p_{rms}$  along with linear least-squares curve fits in Figure 9 for four different sensor diameters. The thickness of the foil utilized in the tests was 8 $\mu$ m. The sensitivity of the largest sensor is 0.62 $\mu$ m/Pa. For reference, this value may be compared to the  $7.68 \times 10^{-5}$   $\mu$ m/Pa mechanical sensitivity of the optical lever-type microphone of Zuckerwar *et al.* (1995). This demonstrates the high flexibility of the LDM's sensor diaphragms used here. Such a high flexibility, which is required in order to produce a resolvable Doppler signal<sup>1</sup> is maintained through the use of polymer, rather than metallic, foils in conjunction with low foil tension (approximately 3.5N/m for the 6.35mm sensor, as estimated using equation [5] below).

Another observation that may be made from Figure 9 is the strong dependence of  $K_x$  on the sensor diameter. From a theoretical point of view, unsteady pressure fluctuations with wavelength that is much larger than the diameter of the sensor produce vibration amplitude at the circular membrane center that is given by (e.g., see Kinsler *et al.*, 1982):

$$x = \frac{d^2}{16\tau} p \quad [5]$$

---

<sup>1</sup> see section V.A. for a discussion of the stringent resolution requirement of the LDM



where  $\tau$  is the foil tension force per unit circumferential width. Hence one would expect  $K_x = x/p$  to increase in proportion to the quadratic power of the diameter. To compare this to the observed experimental trend, the sensitivity of different size sensors was obtained from the linear curve fits in Figure 9. These values were then plotted in units of dB ( $20 \log K_x$ ) versus the logarithm of the diameter in Figure 10 together with a trend line corresponding to the quadratic dependence on diameter. Note that error bars were included in Figure 10 to reflect the variability of  $\tau$  values, which were not controlled during adhesion of the sensor membrane to the substrate. These values were calculated by substituting each sensor's diameter and measured sensitivity in equation [5]. The error bars were then estimated as twice the *rms* variation in  $\tau$ . As depicted from the figure, the dependence of the measured sensitivities on sensor diameter is consistent with the theoretical trend, within the uncertainty of the measurements.

*VI.B. Accuracy.* In order to estimate the sensor's accuracy, the effect of various types of error on the sensor output needs to be assessed. To this end, it is desired to obtain many calibrations of the sensor when subjected to increasing as well as decreasing pressure. To accomplish this, 500 data points resulting from ten repeated cycles of pressurization/depressurization of the sensor's membrane by 200Hz sound waves in the PWT are used. These data may be seen in Figure 11, where the pressure is plotted versus the membrane deflection for a 6.35-mm sensor. Note that since the data are obtained under dynamic conditions, the small phase shift that exists between  $p$  and  $x$  at 200Hz is removed prior to plotting the data (see section *VI.C* for more details on the sensor's phase response).

Figure 11 (top) displays the sensor calibration, when subjected to pressure in the range  $-3\text{Pa} < p < 3\text{Pa}$ . A straight line fit of the data is also included in the figure. Clearly, the sensor response follows the fit very closely. Any possible non-linearity is less than the random data

scatter around the fit. This scatter represents a repeatability error ( $\epsilon_r$ ), which is estimated to be within  $\pm 3\%$  of the full-scale pressure based on the standard error of the fit.

When the range of pressure change is increased to  $-10\text{Pa} < p < 10\text{Pa}$ , the sensor's response exhibits some non-linear behavior, as evident from Figure 11 (bottom). In particular, a third-order polynomial fit seems to represent the data more closely than the linear fit obtained over the narrower pressure range in the top part of Figure 11. The difference between the two fits is used to calculate the non-linearity error ( $\epsilon_n$ ). The results yield an *rms* non-linearity error of 5.4% of full scale pressure. The corresponding value of  $\epsilon_r$  is 1% for this larger pressure range.

On the other hand, the sensor hysteresis is examined by taking one cycle of the pressure and displacement time series and plotting them against each other in Figure 12. As seen from the figure, no systematic difference in the sensor's response is observed during the pressure-increase phase in comparison to the pressure-decrease phase. Any differences are random and less than the repeatability error.

The combination of the repeatability, non-linearity and hysteresis errors, results in an overall error that is less than 7% of full scale pressure for the 6.35-mm sensor and pressure amplitude less than 10Pa. That is, the measurement accuracy of this sensor is better than 93%, which is well within the  $\pm 2\text{dB}$  tolerance band typically associated with microphone sensitivity/bandwidth specification. For the smaller sensors, an even better accuracy was obtained for the same pressure range, as the non-linearity error (the dominant component in the above estimate) was less than 2%.

*VI.C. Bandwidth.* Figure 13 displays the sensor frequency response ( $K_x$  and  $\phi$ ) for 6.35, 3.175 and 1.587mm LDM sensors. Included in Figure 13 (top) are broken lines indicating  $\pm 2\text{dB}$  variation relative to the sensitivity of each sensor. Except for one apparently errant data point,

the frequency response for all sensors is flat up to the neighborhood of the resonant peak. This peak is depicted at approximately 2kHz for the 6.35mm sensor, while for the smaller sensors the resonant peak is not captured within the test frequency range. This is consistent with the phase shift results of the different sensor sizes shown in Figure 13 (bottom). More specifically, the 6.35mm sensor is the only sensor for which the phase angle goes through an abrupt transition from zero to 180 degrees within the frequency range of the test. Such a transition is known to occur in the vicinity of the sensor's resonance frequency.

The increase in resonant frequency with decreasing diameter follows the expected theoretical trend for natural vibrations of a circular membrane fixed at the rim. Namely, the resonant frequency ( $f_r$ ) for the fundamental mode of vibration of the membrane is given by (e.g., Kinsler *et al.*, 1982):

$$f_r = \frac{2.405}{\pi d} \sqrt{\frac{\tau}{\rho_s}} \quad [6]$$

where  $\rho_s$  is the surface mass density of the foil (i.e., the mass per unit area). Thus, for approximately the same tension and similar surface mass density, one would expect the resonant frequency to increase with decreasing sensor size.

The large resonant peak observed for the 6.35mm microphone limits the sensor's bandwidth significantly. For example, within the  $\pm 2$ dB tolerance, Figure 13 shows a bandwidth that extends to approximately 800Hz for the 6.35mm sensor. This bandwidth can be increased by damping the air motion induced by foil oscillation inside the sensor hole. In the current investigation, this was accomplished by gluing multiple layers of lens-cleaning paper on the backside of the faceplate. Since this type of paper is porous, it allows air flow with some resistance that increases with the number of layers utilized. The resulting effect on the sensor's

response is depicted in Figure 14, where the frequency response of a 6.35mm sensor is displayed with and without the use of the damping material. Note that the specific sensor used to obtain the results in Figure 14 is different from the same size sensor used to generate Figure 13. The sensor in Figure 14 has a slightly higher resonant frequency and a bandwidth that extends to approximately 1000Hz. As seen from Figure 14 (top), the sensor's resonant peak is attenuated substantially such that it almost falls within the  $\pm 2\text{dB}$  band when 8 layers of damping paper are used. This extends the sensor's bandwidth to approximately 3000Hz. Also note that the increased damping results in more gradual phase rise around the resonance frequency.

*VI.D. Foil Thickness and Material Effect.* The thickness of the foil material is expected to affect two aspects of the LDM's response. The first of these is a direct effect whereby the surface mass density increases in linear proportion to the thickness. The second one relates to the established foil tension. It seems reasonable to expect that using the same technique to mount different foils results in comparable local radial strain, and hence stress, in the foil. When the stress is multiplied by the foil thickness, one obtains  $\tau$  in dimensions of force per unit length. Thus,  $\tau$  is expected to be a linear monotonic function of the foil thickness.

This monotonic dependence when coupled with equation [5], one would expect that  $K_x$ , for the same-diameter, same-material sensor, decreases with increasing diaphragm thickness. This conclusion agrees well with the frequency response results shown in Figure 15 for a 6.35mm sensor. Two of the three response curves depicted in the figure pertain to two different foil thickness (5 and 12 $\mu\text{m}$ ) of the same material (PET). The sensitivity of the thicker foil is 2.8 times less than that of the thinner one, which is of the order of the 2.4 thickness ratio. On the other hand, equation [6] shows that the linear variation of both  $\tau$  and  $\rho_s$  with foil thickness should cancel out, and hence the sensor's resonant frequency should remain unchanged. This

seems to be approximately the case where the resonant peak of the 12 $\mu$ m-thick sensor is seen to be slightly larger than that of the 5 $\mu$ m-thick one in Figure 15. This difference is most likely due to the uncontrolled variability in the initial foil strain inherent to the foil adhesion process. The same variability is also believed to be responsible for the discrepancy between the predicted sensitivity change of 2.4 and the actual one of 2.8.

Figure 15 also demonstrates the effect of using a more flexible material. Recalling that the modulus of elasticity for PP is about 1.3 – 4 times less than that of PET, one would expect that the stress, and hence  $\tau$ , would be 1.3 – 4 times smaller for a foil made of PP than PET. A corresponding increase in  $K_x$  for the former is also expected. This increase is partially offset by the thicker PP foil (8 $\mu$ m) used for the results in Figure 15. Thus, a sensitivity increase in the range of 0.8 – 2.5 (-2 – 8.0dB) is anticipated for the 8 $\mu$ m over the 5 $\mu$ m foil in Figure 15. This is consistent with the roughly 6dB higher sensitivity of the PP-based sensor seen in the figure. Also, when accounting for the differences in both thickness and density of the foil for the two sensors,  $\rho_s$  for both foils is found to be approximately the same. Therefore, the PP-foil sensor, with its smaller  $\tau$  value, should have a lower resonant frequency (see equation [6]), which is the case as evident from Figure 15. In fact, the ratio of the two resonant frequencies is approximately 1.4 (2922 and 1976Hz for the 5 and 8  $\mu$ m-thick sensors, respectively). Referring to equation [6], one may then deduce that  $\tau$  is twice (a factor of 6dB) as large for the thinner PET foil. This is consistent with the 6dB sensitivity difference between the two sensors.

*VI.E. A Note on Foil Adhesion Procedure.* As discussed in section III.A, for all tests conducted here, the LDM's diaphragm was mounted on a faceplate with the appropriate hole size using water adhesion forces. This seemed to hold the foil firmly to the faceplate with very little change in sensor characteristics for at least few hours. To further verify that the characteristics

of water-adhered sensors are commensurate with their epoxy-adhered counterpart, the frequency response of a sensor of the former type was compared to that of the latter for 3.175mm sensor. The results are shown in Figure 16. As depicted in the figure, the response of both sensors is quite comparable. This verifies the utility of water in constructing LDM sensors for laboratory measurements.

*VI.F. Projection of LDM Use for High-Reynolds-Number Wall-Bounded Flow Measurements.* As mentioned in the introduction, an important motivation of the current work is the potential to realize high-spatial-resolution wall-pressure-measurements beneath high-Reynolds-number turbulent boundary layers. Therefore, it was desirable to capitalize on the findings of the current investigation to assess this potential. To this end, the  $K_x$  values determined for the 5 $\mu$ m-thick PET foil for different sensor sizes were employed to estimate an average sensor tension of 15N/m. By using this value in conjunction with equation [5],  $K_x$  for the following sensor diameters was obtained: 0.1, 0.25, 0.5, 1 and 2mm. The resulting sensitivities were then substituted in equation [4] to yield the NEP spectrum for different  $d$  magnitudes. These spectra are shown in Figure 17 using solid lines, along with three different turbulent-boundary-layer wall-pressure spectra at different Reynolds numbers based on momentum thickness ( $Re_\theta$ ).

The lowest Reynolds number spectrum shown in Figure 17 was obtained from measurements in a low-speed wind tunnel at Michigan State University (MSU) using an electret microphone. The two higher-Reynolds-number ones were estimated based on accepted scaling of the spectra at the high-frequency end (e.g., see Farabee and Cassarella, 1991, and Gravante *et al.*, 1998), and measured and estimated boundary layer parameters, for  $Re_\theta = 22000$  and  $Re_\theta = 35000$ , respectively. These two cases correspond to flow situations that could be established in

the National Diagnostics Facility (NDF) at Illinois Institute of Technology (Hites, 1997), and the Navy's Large Cavitation Channel (LCC). Note that in estimating the spectra for both situations it has been assumed that the Reynolds number dependence manifests itself as widening of the overlap region of the spectrum, which scales on both the viscous and momentum-thickness length scales and exhibits  $f^{-1}$  frequency dependence. Also, it is important to realize that wall-pressure spectra at equal Reynolds numbers will not necessarily coincide when plotted in Figure 17. The spectrum plot for a given Reynolds number depends also on the friction velocity and fluid density. However, the cases shown in the figure give broad representation of boundary layer flows attainable in high Reynolds number air and water test facilities, which is sufficient for the purposes of the current estimation exercise.

Referring to Figure 17, the useful frequency range of a sensor of a given size is that for which the corresponding boundary-layer wall-pressure spectrum rises above the NEP spectrum (note that NEP lines have been truncated at the corresponding estimated resonant frequency). For the lowest Reynolds number case, it seems that at least a 1mm diameter sensor must be used to capture most of the displayed spectrum. Hence, the LDM size can't be made too small for low-Reynolds-number measurements. This stems from the fact that the wall-pressure fluctuations at low Reynolds numbers are extremely small (*rms* is typically of the order of a fraction to one Pascal) and hence are not capable of overcoming the sensor's own noise.

On the other hand, sensors as small as 0.1mm are usable for  $Re_\theta = 22000$  case. In particular, the NEP spectrum intersects the wall-pressure spectrum for this case at  $f \approx 50\text{kHz}$ , which is approximately one-half of the viscous frequency scale ( $\nu/u_\tau^2$ ;  $u_\tau = 1.27\text{m/s}$  for this case). On the lower frequency end, the 0.1mm sensor is seen to resolve practically all of overlap region (Figure 17), which should contain most of the fluctuations at such a high Reynolds

number. The corresponding  $d^+$  value for this sensor is 8.5, which is well below the order of 20 required for good resolution of the spectrum. If it is desired to conduct measurements at frequencies below the lower-end of the  $f^{-1}$  region, one could use larger size sensors since spatial averaging is not a concern for this frequency range.

Finally, for the estimated boundary layer case in the LCC ( $Re_0 = 35000$ ), a frequency range comparable to that captured by the 0.1mm sensor in the  $Re_0 = 22000$  case is measurable using 0.25mm sensor. The corresponding non-dimensional diameter is  $d^+ = 20$  ( $u_\tau$  estimate being 0.08 m/s in this case). Higher Reynolds number boundary layers in the LCC (achieved by increasing the freestream velocity) should possess spectra that are shifted higher and to the right of the one corresponding to  $Re_0 = 35000$ . Thus, as the Reynolds number is increased, sensors smaller than 0.25mm should be usable to resolve the correspondingly smaller viscous length scales. The LCC and IIT examples serve as a demonstration that in fact the LDM sensor concept is one that is inherently suited for high-spatial-resolution diagnostics beneath high-Reynolds-number flows.

Finally, in addition to its better spatial resolution, another inherent advantage of the use of the Doppler transduction scheme for measurements at high frequency is that the *primary* sensor output, in response to the pressure input, is the *velocity*, and not the *displacement* of the sensor's membrane. More specifically, for a given displacement amplitude of the membrane, the velocity increases linearly with increasing frequency. That is, the sensor *primary* sensitivity increases linearly with frequency, thus it would possess a better signal-to-noise ratio than existing microphone technology at high frequencies.

A demonstration of the better signal-to-noise ratio of the LDM over typical existing microphone technology at higher frequencies was obtained in a wind tunnel test. In the



demonstration, an LDM sensor was mounted side by side with a commercial Panasonic electret microphone in the side of a wind tunnel test section. A 12.5 mm fence was installed perpendicular to the test section sidewall upstream of the sensors such that the mean flow reattachment location roughly coincided with the position of the microphones. The wall pressure spectra from both sensors were obtained and the results are displayed in Figure 18. It is evident that the LDM results agree well with those obtained from the Panasonic sensor in the middle range of frequencies. At frequencies below 100 Hz, the LDM suffers from low signal-to-noise ratio as anticipated, and the two spectra deviate substantially. However, at the high frequency end of the spectrum, the pressure fluctuations are too weak to overcome the background level of the Panasonic microphone, as its spectrum 'flattens out'. In contrast, the LDM spectrum continues smoothly as expected from turbulent-type wall-pressure fluctuations.

## VII. CONCLUSIONS

A new optical unsteady-wall-pressure sensor has been developed and characterized. The sensor's principle of operation is based on the Doppler frequency shift associated with the reflection of a focused laser beam off a metalized flexible polymer diaphragm. Prototypes of the sensor were characterized in a plane wave tube over the frequency range  $50 < f < 5000\text{Hz}$ . The results revealed a sensor deflection sensitivity that ranged from  $0.002\mu\text{m}/\text{Pa}$  to  $0.74\mu\text{m}/\text{Pa}$  for sensor diameters in the range of 0.794 – 6.35mm and 8 $\mu\text{m}$ -thick PET diaphragm. The corresponding resonant frequency was found at 2000Hz for the largest sensor, increasing beyond the tested frequency range with decreasing sensor diameter. Both the sensitivity and bandwidth depended on the diaphragm's material and thickness.

Finally, it was demonstrated, by using estimates of typical wall-pressure spectra in two high-Reynolds-number facilities (NDF at IIT and Navy's LCC), that the Doppler sensor could be

used successfully for measurements of the wall-pressure beneath turbulent boundary layers in these facilities with sufficient spatial resolution. Thus, the technique offers good basis for a new high-Reynolds-number diagnostics tool.

#### **VIII. ACKNOWLEDGEMENT**

This work is supported by grant number N00014-99-1-0858 from the Office of Naval Research, monitored by Dr. L. Patrick Purtell.

## IX. FIGURES

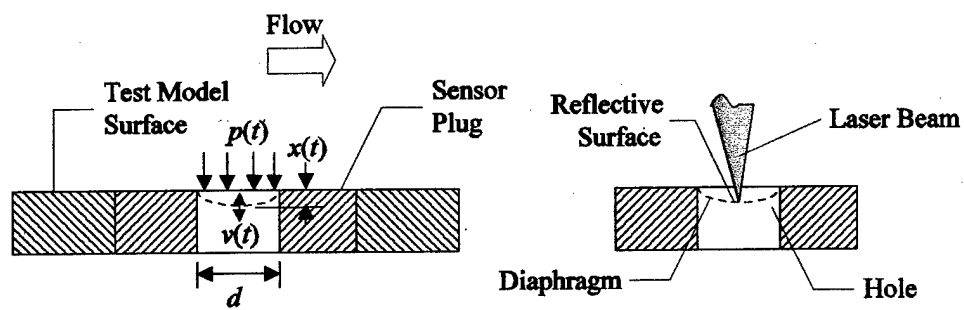


Figure 1. Terminology and principle of LDM sensor

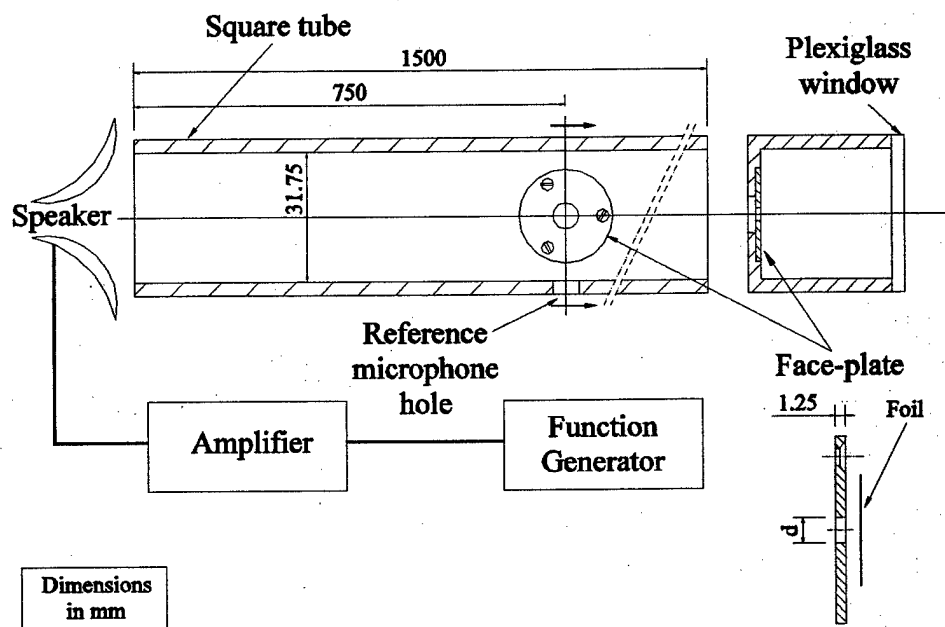


Figure 2. Schematic of the Plane Wave Tube setup and the LDM sensor plug

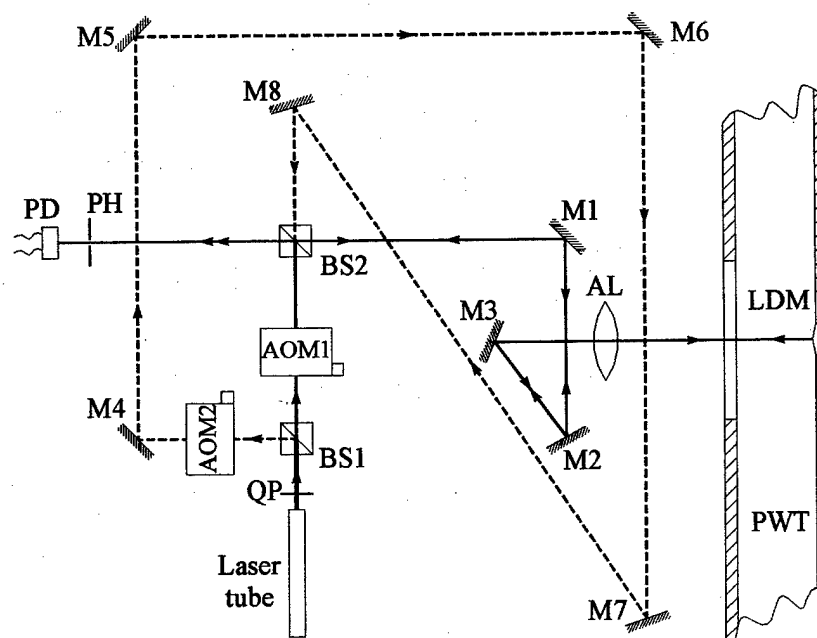
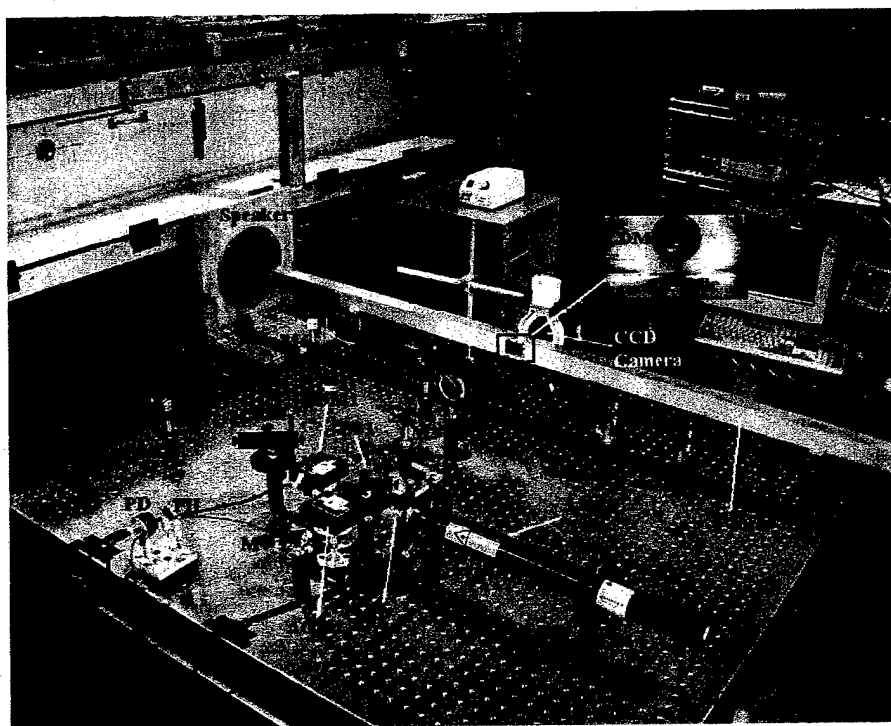


Figure 3. Photograph of the optical system setup (top) and corresponding ray-trace diagram (bottom)

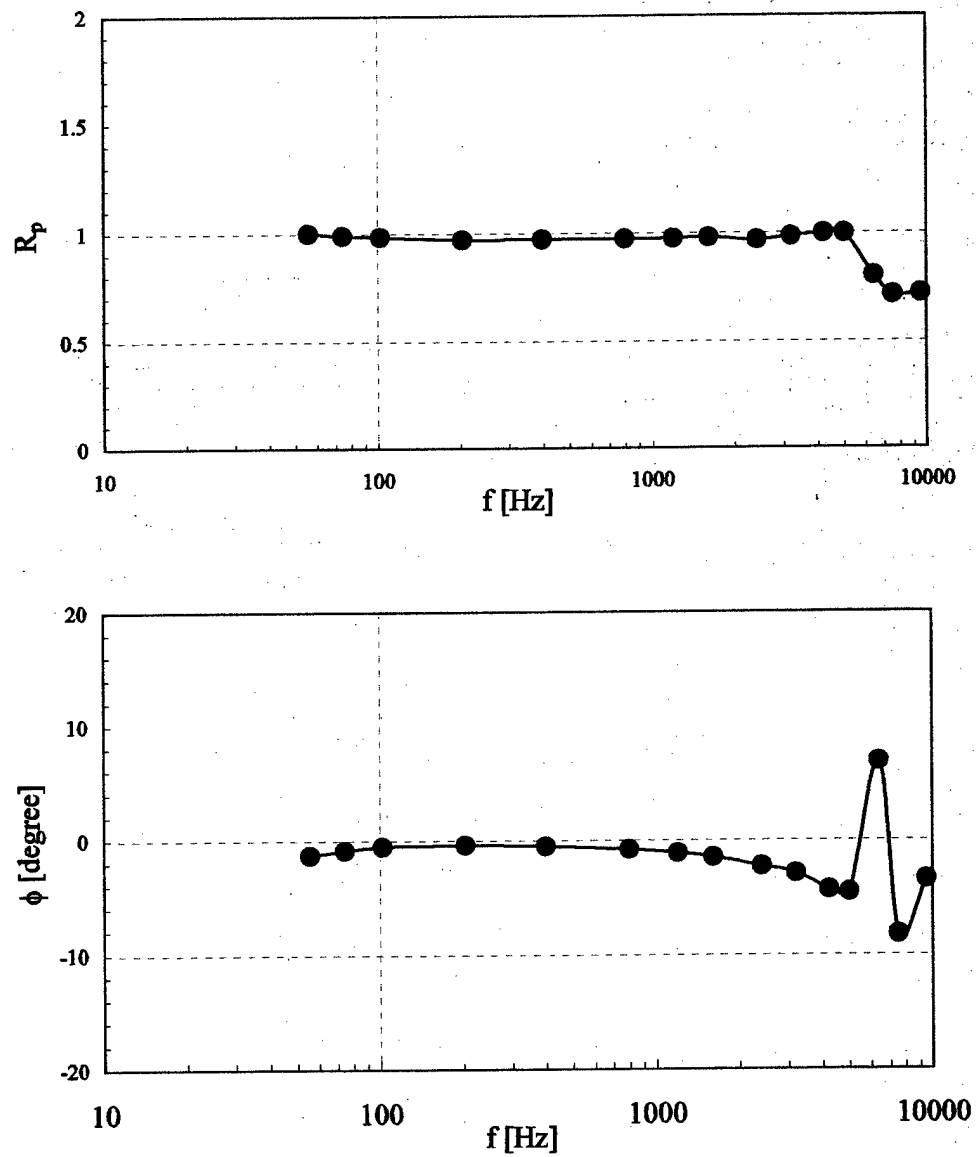


Figure 4. PWT calibration test: *rms* pressure ratio (top) and phase (bottom) results

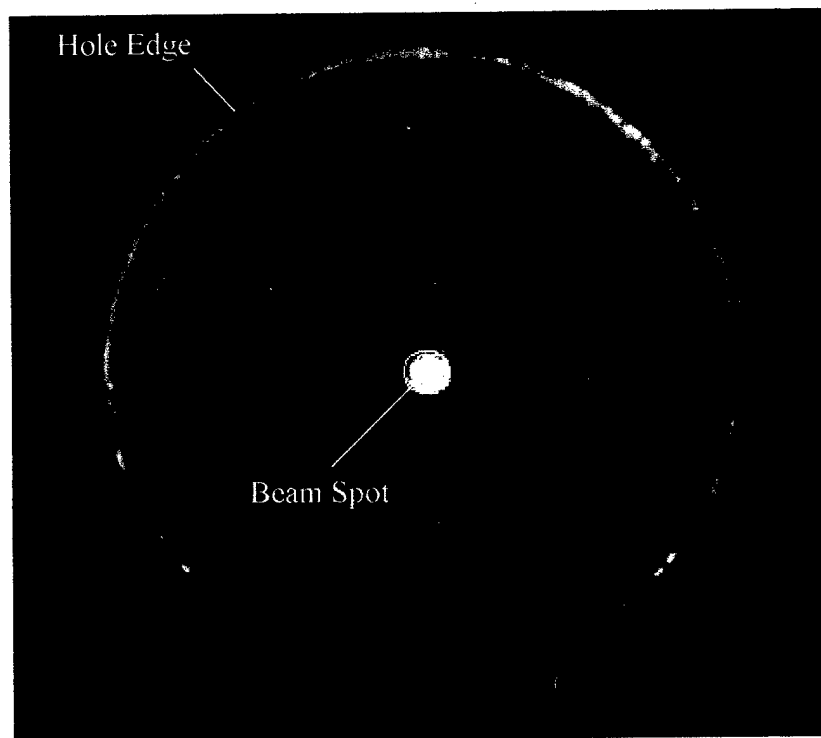


Figure 5. A sample image of a centered beam

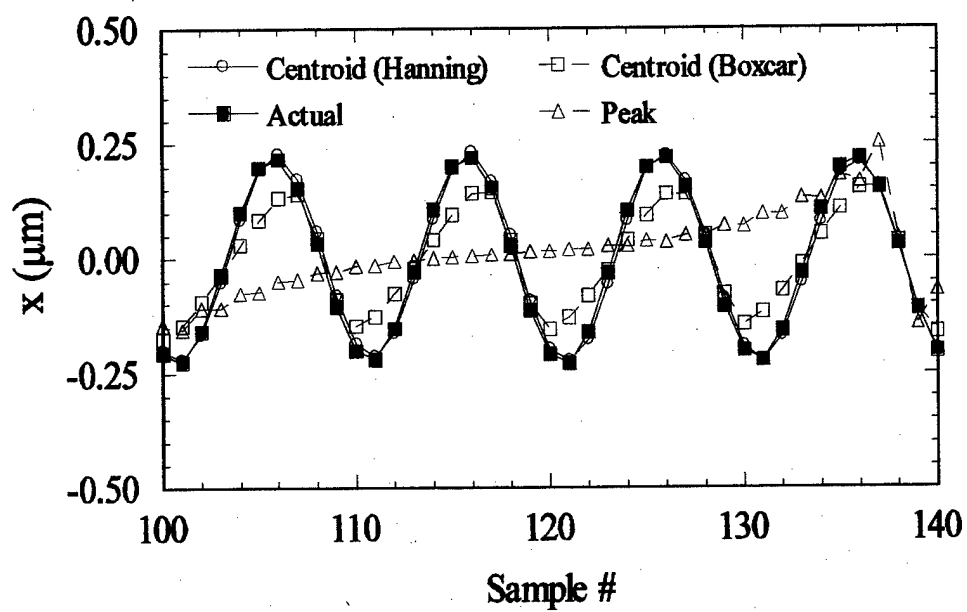


Figure 6. Demonstration of Doppler-frequency-resolution effect on the measurement signal



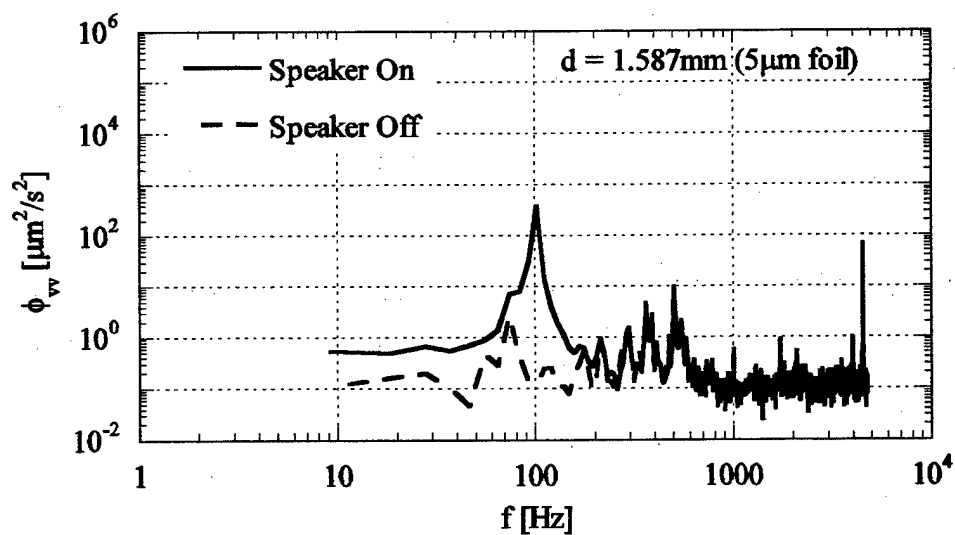
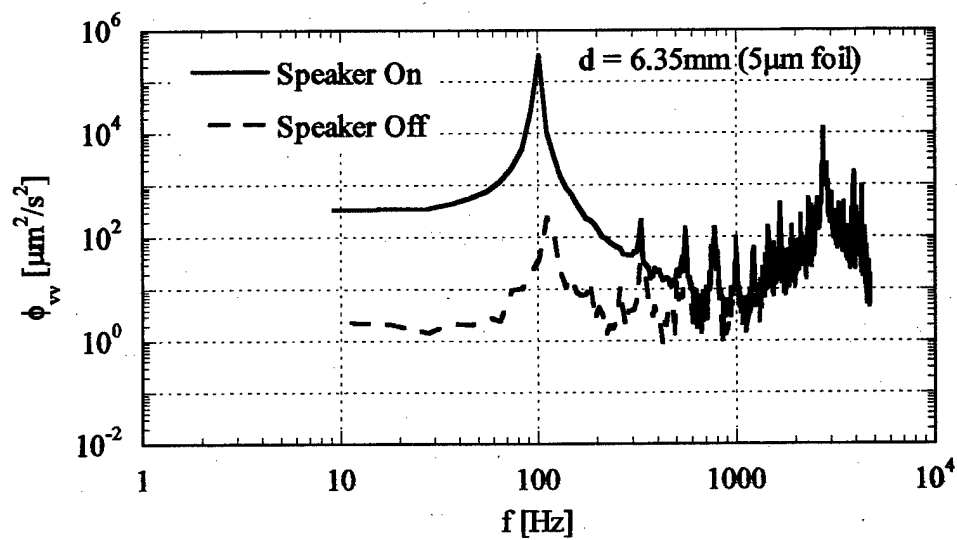


Figure 7. Signal and noise spectra for 6.35mm (top) and 1.587mm (bottom) sensors

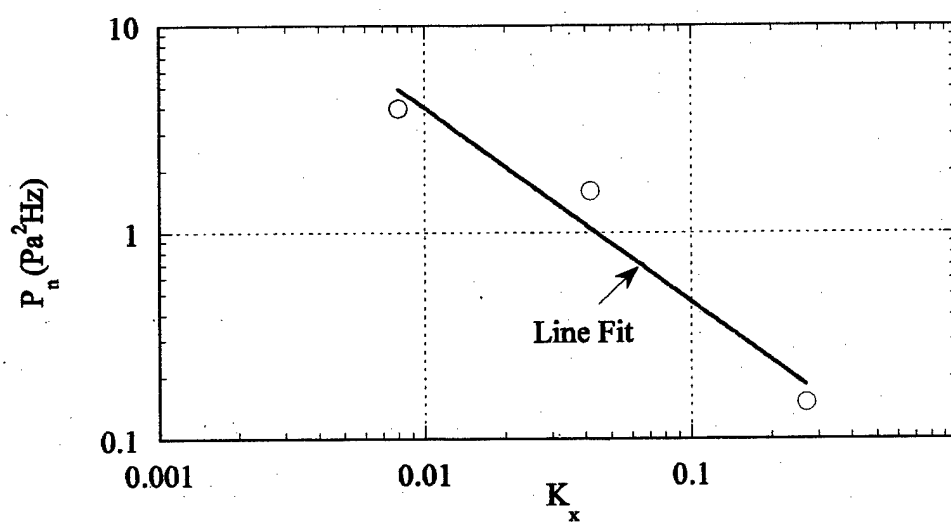


Figure 8. Effect of sensor sensitivity on noise

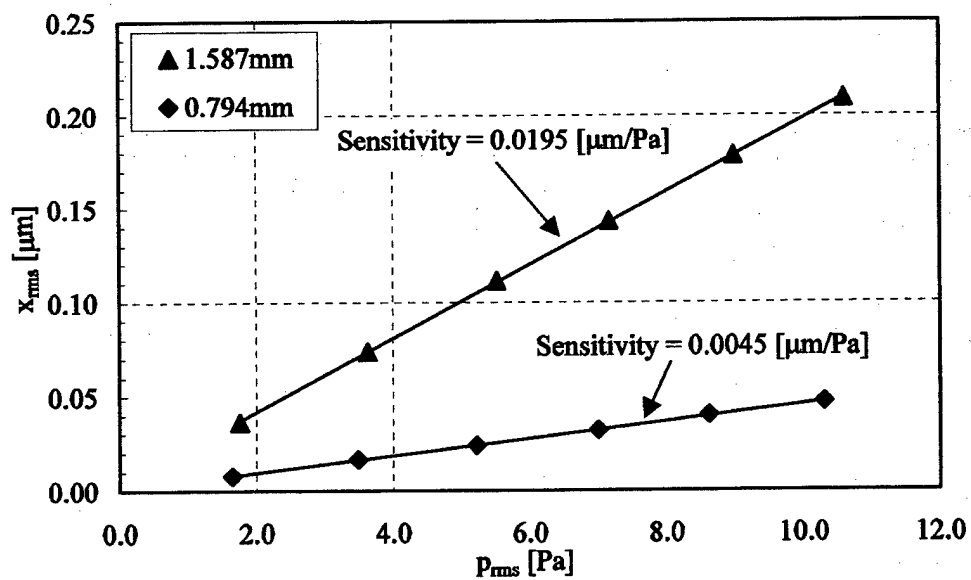
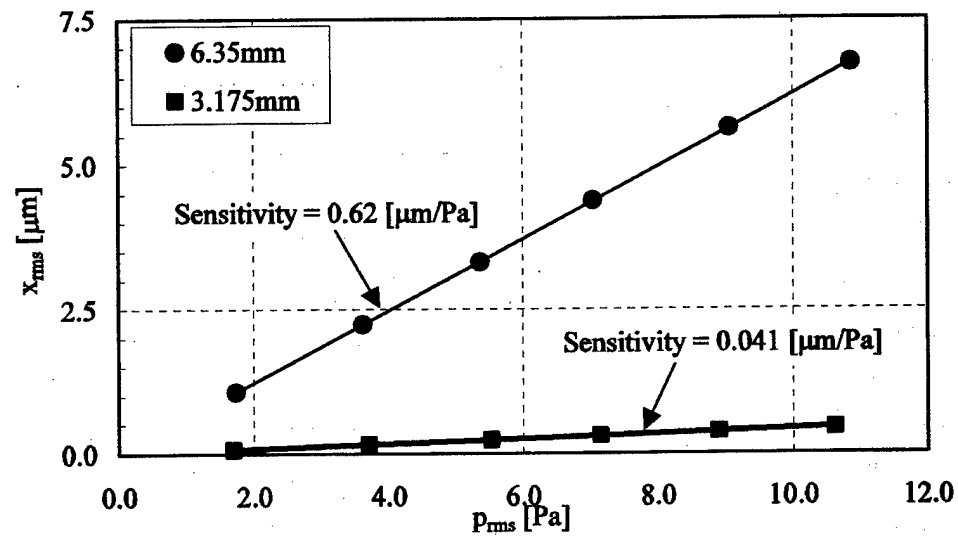


Figure 9. Calibration of different-size  $8\mu m$ -foil LDM sensors at 200Hz sound frequency

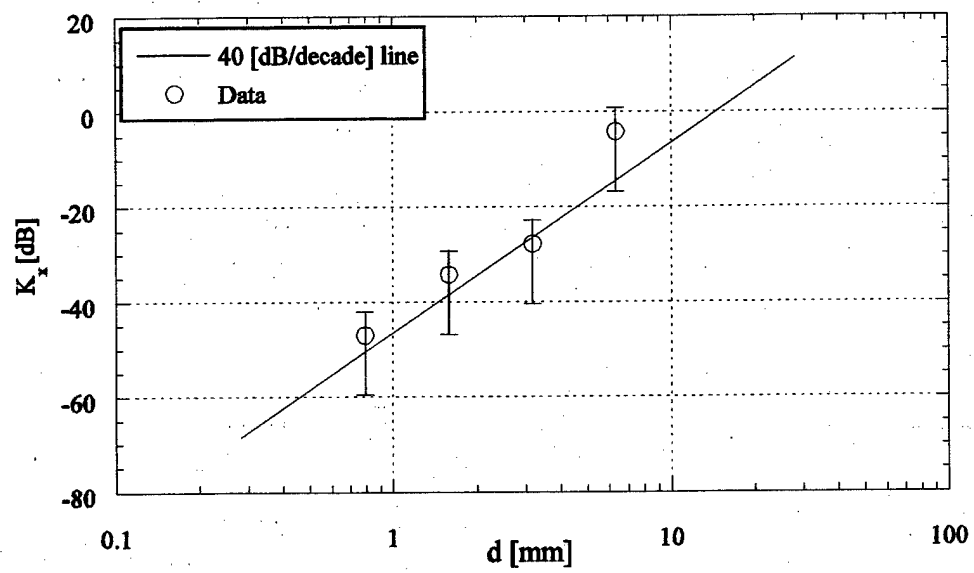


Figure 10. Effect of sensor size on  $K_x$

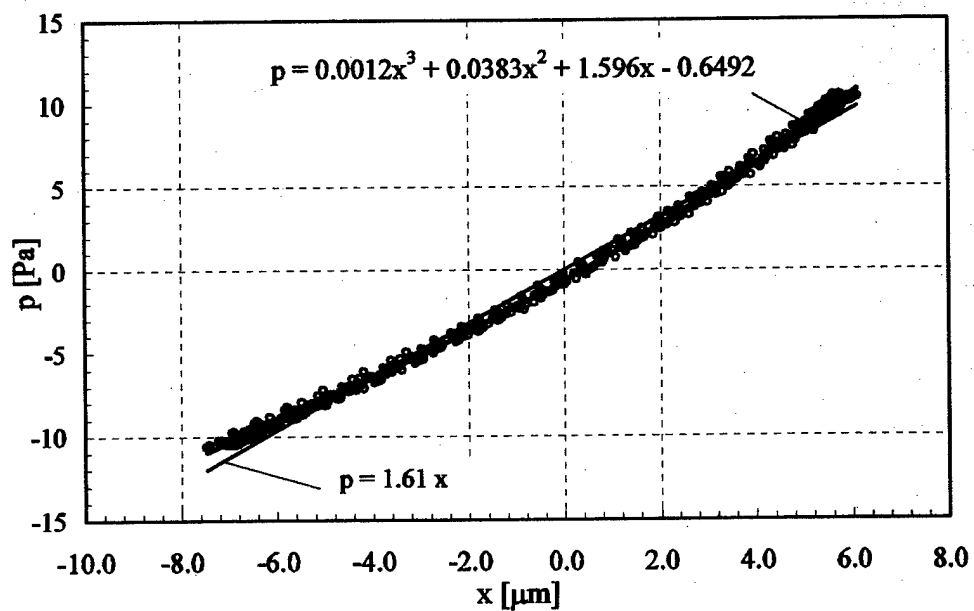
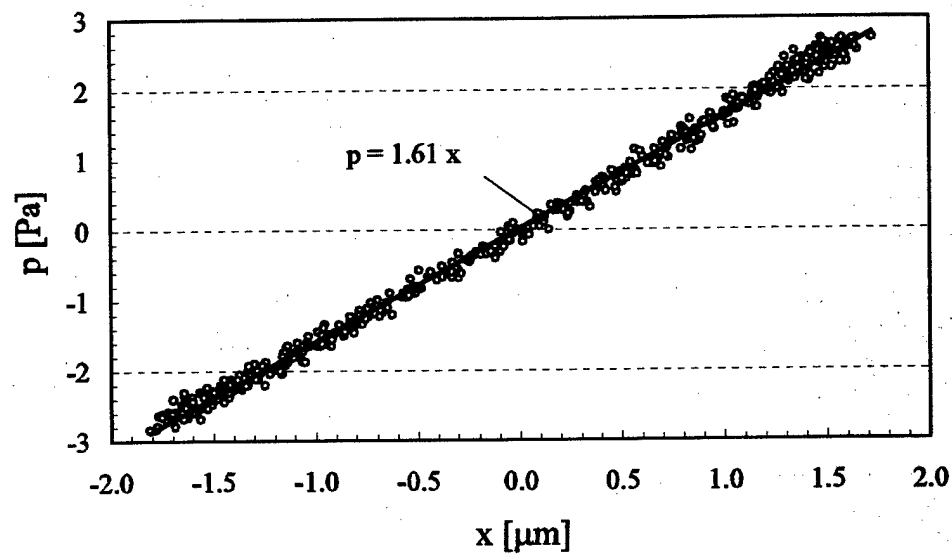


Figure 11. Pressure-deflection characteristics for 6.35mm sensor over the range:  $-3\text{Pa} < p < 3\text{Pa}$  (top), and  $-10\text{Pa} < p < 10\text{Pa}$  (bottom)

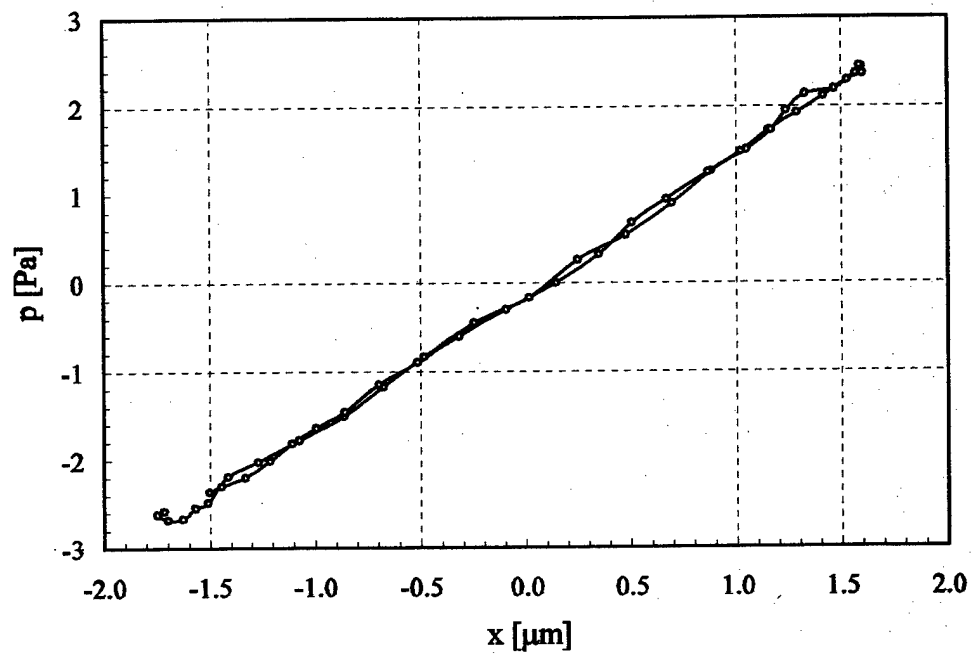


Figure 12. Sensor Hysteresis

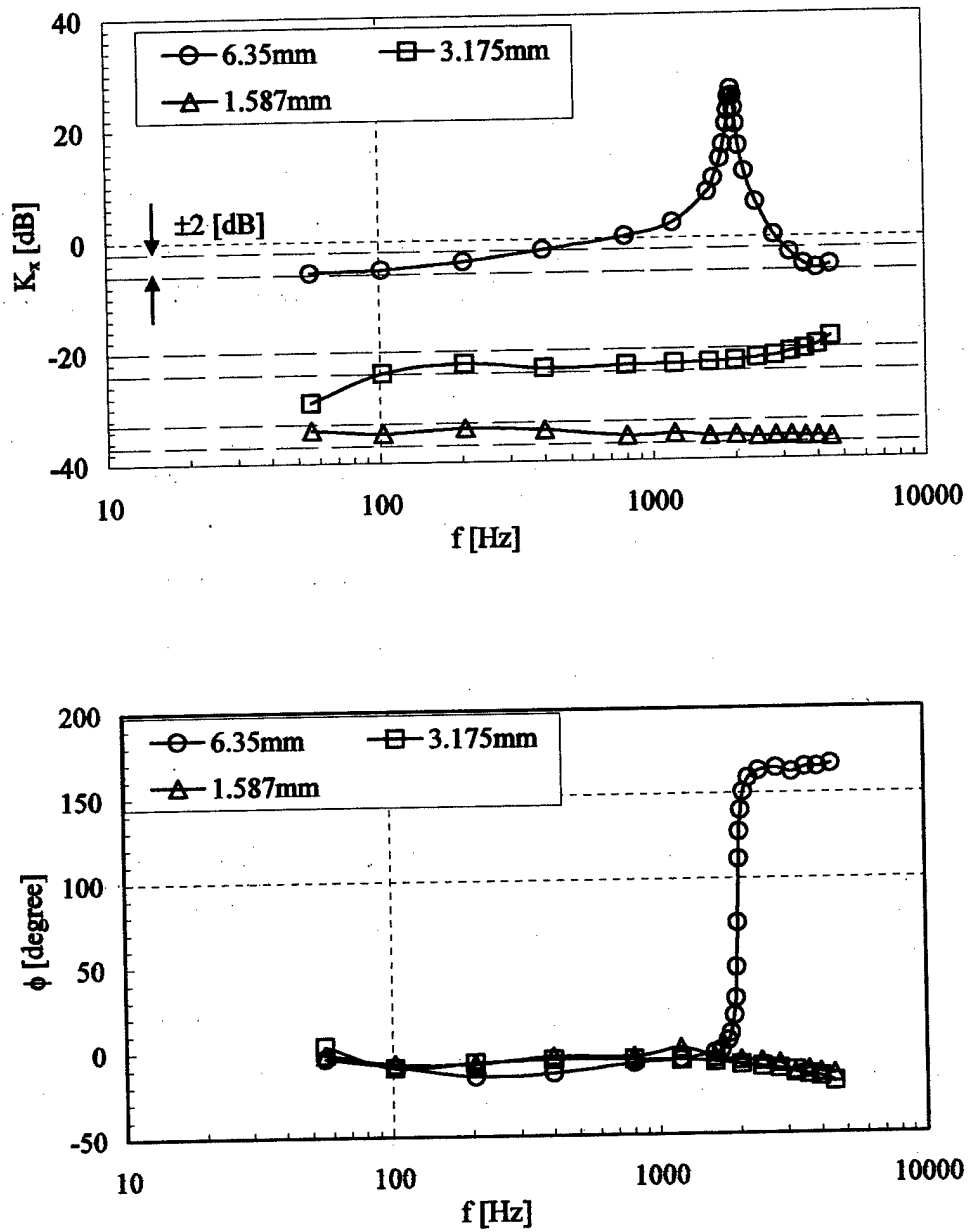


Figure 13. Frequency response for three different sensor sizes with  $8\mu\text{m}$  foil thickness:  
sensitivity (top) and phase shift (bottom)

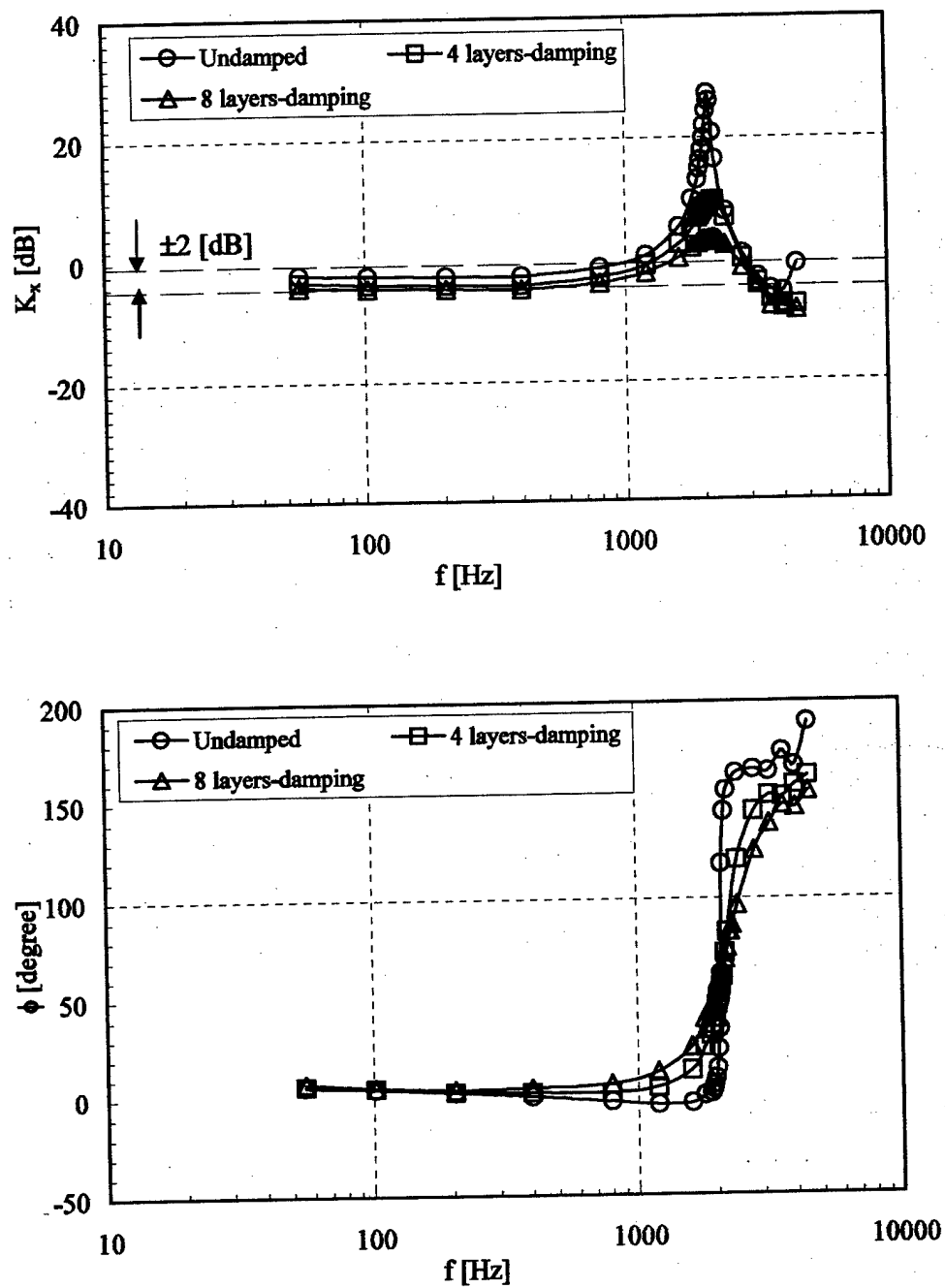


Figure 14. Effect of damping on the frequency response of 6.35mm sensor with 8 $\mu$ m-thick foil: sensitivity (top) and phase shift (bottom)



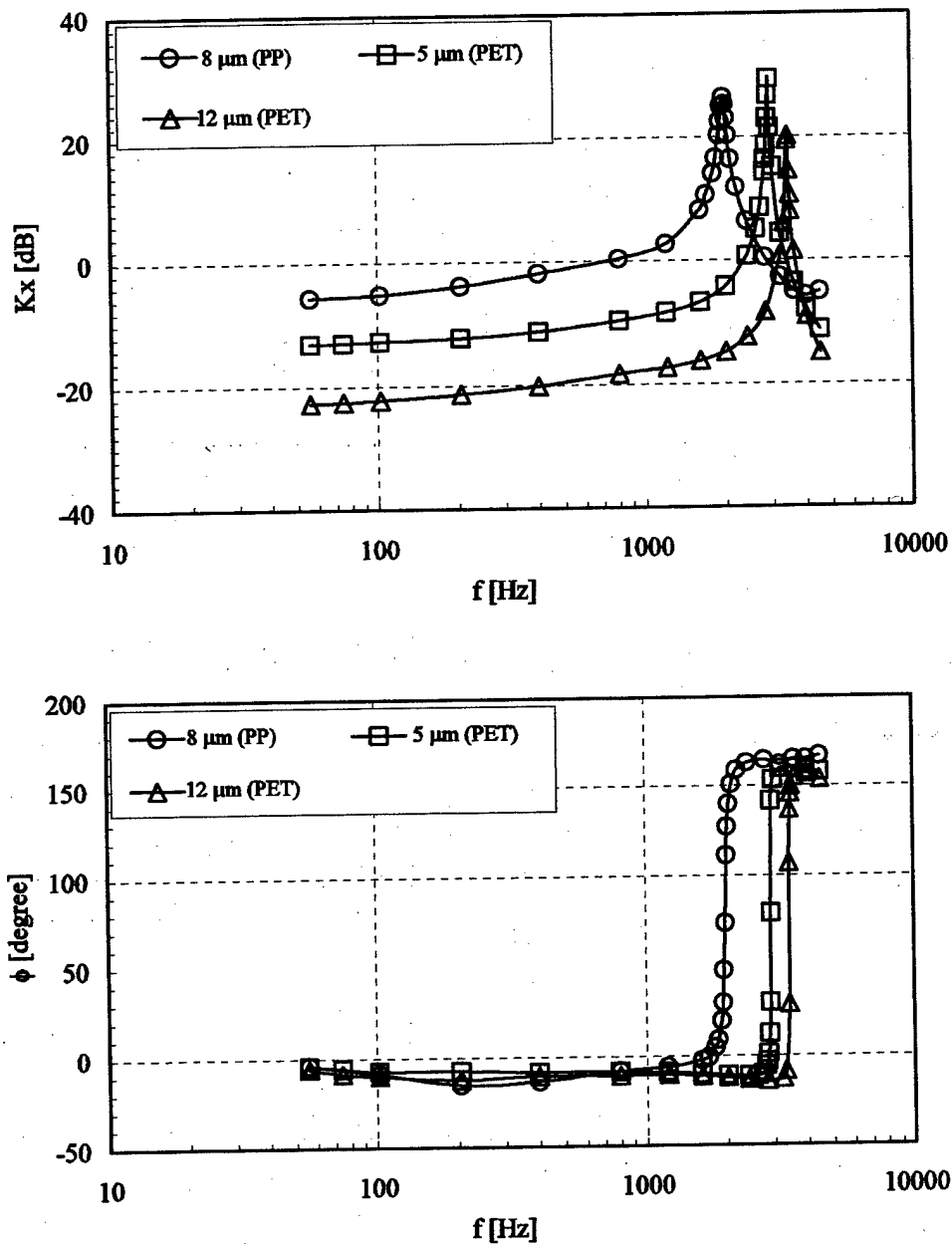


Figure 15. Effect of diaphragm thickness and material on LDM frequency response: sensitivity (top) and phase shift (bottom)

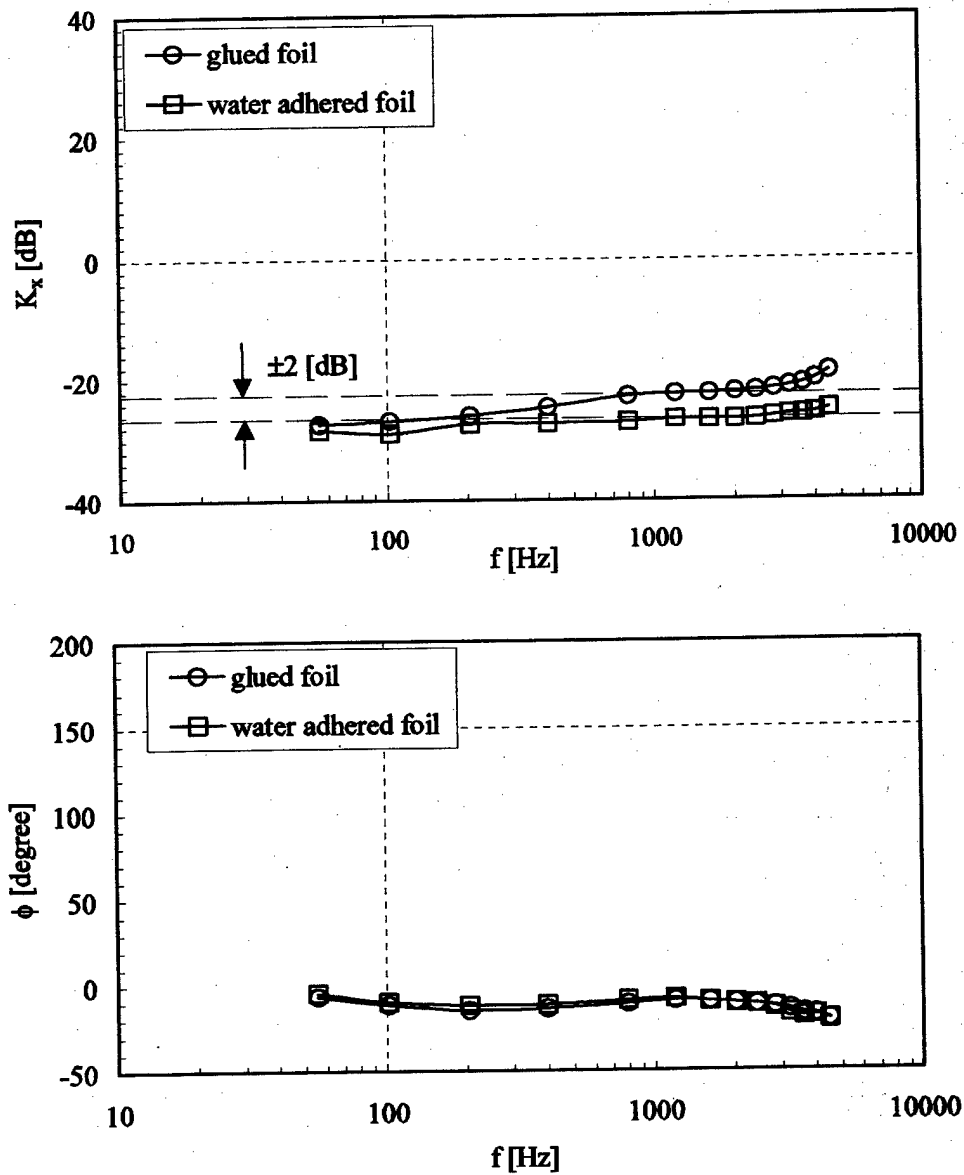


Figure 16. Comparison between the frequency response of water- and epoxy-adhered diaphragms: sensitivity (top) and phase shift (bottom)

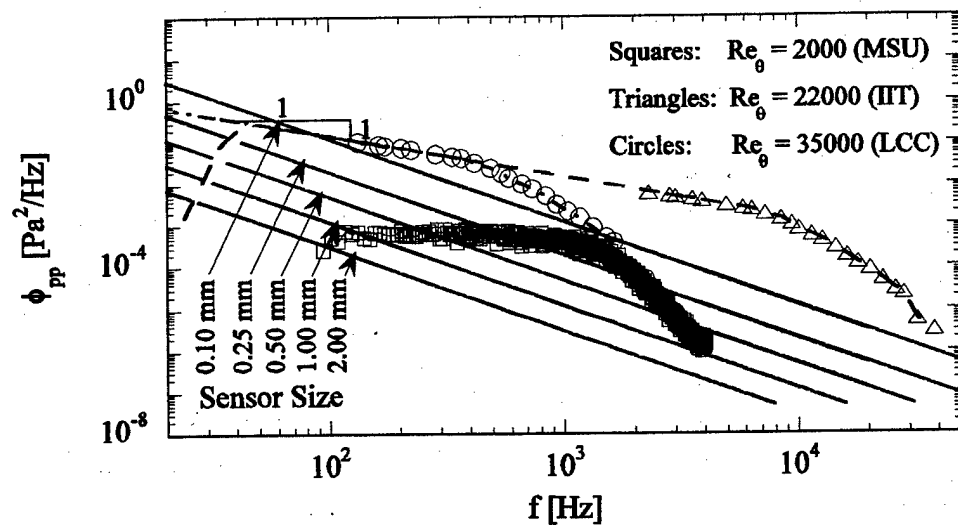


Figure 17. Plot for assessment of sensor usability for measurement beneath turbulent boundary layers at different Reynolds numbers

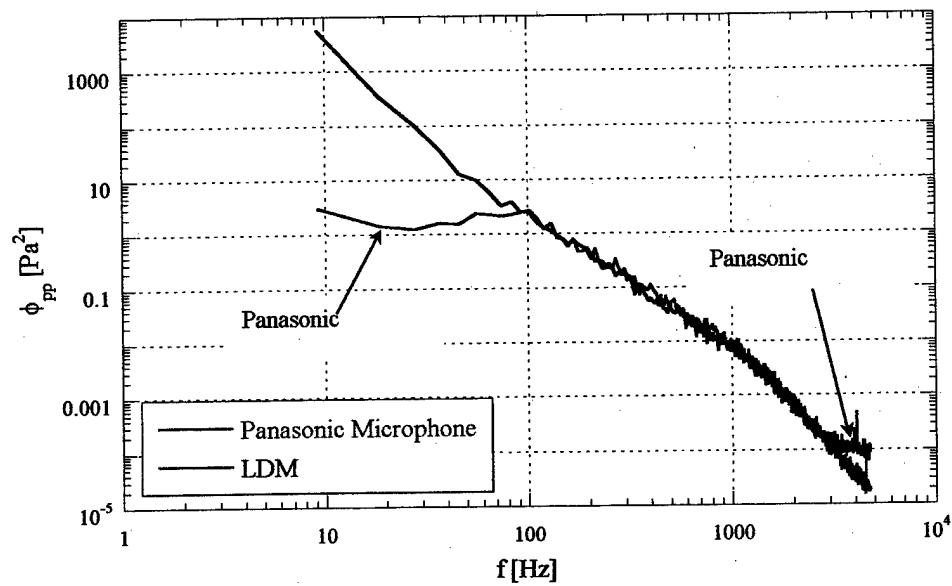


Figure 18. Comparison between LDM and Panasonic measured spectra

## X. REFERENCES

- Bucaro J.A., Lagakos N., Cole J.H. and Giallorenzi T.G. 1982, "Fiber Optic Acoustic Transduction," Physical Acoustics, edited by Mason J.P. and Thurston R.N., **XVI**, Academic, New York.
- Daoud M. and Naguib A. 2003, "A Doppler Sensor for High Spatial Resolution Measurements of Unsteady Surface Pressure," *Meas. Sci. Technol.*, **14**, 13.
- Emmerling R. 1973, "The Instantaneous Structure of the Wall Pressure Under a Turbulent Boundary Layer Flow," Ber. - Max Plank Inst. Stromungsforsch., **9**.
- Farabee T.M. and Casarella J.J. 1991, "Spectral Features of Wall Pressure Fluctuations Beneath Turbulent Boundary Layers", *Physics of Fluids*, **3**, 2410.
- Gravante S., Naguib A., Wark C. and Nagib H. 1998, "Characterization of the Pressure Fluctuations Under a Canonical Turbulent Boundary Layer," *AIAA Journal*, **36** (10), 1808.
- He G. and Cuomo F.W. 1991, "A Light Intensity Function Suitable for Multi-mode Fiber-Optic Sensors," *J. Lightwave Technol.*, **9**, 545.
- Hites M. 1997, "Scaling of High-Reynolds-Number Turbulent Boundary Layers in the National Diagnostics Facility," Ph.D. Thesis, Illinois Institute of Technology, Chicago, IL.
- Hixon L.E. and Bush-Vishniac J.I. 1998, "Transducer Principles," Chapter 110, *Handbook of Acoustics*, 1375.
- Hudy L.M. 2001, "Simultaneous Wall-Pressure Array and PIV Measurements in a Separating/Reattaching Flow Region", M. Sc. Thesis, Michigan State University, East Lansing, MI.
- Kinsler L.E., Frey A.R., Coppens A.B. and Sanders J.V. 1982, "Fundamentals of Acoustics," Third Edition, John Wiley & Sons.

Naguib A. 2002, "Resolution Enhancement of Doppler Frequency Measurements Using a Centroid Technique," *Exp. Fluids*, **32**, 600.

Zuckerwar A.J., Cuomo F.W., Nguyen T.D., Rizzi S.A. and Clevenston S.A. 1995, "High-Temperature Fiber-Optic Lever Microphone," *J. Acoust. Soc. Am.*, **97** (6), 3605.